L-shell photoionization of Ar^+ to Ar^{3+} ions

C. Blancard,[1,2] Ph. Cossé,[1] and G. Faussurier[1]
[1]*CEA, DAM, DIF, F-91297 Arpajon, France*
[2]*Observatoire de Paris, LUTH, CNRS UMR 8102, 5 place Jules Janssen, F-92195 Meudon, France*

J.-M. Bizau,[3,4,*] D. Cubaynes,[3,4] N. El Hassan,[3,†] S. Guilbaud,[3] and M. M. Al Shorman[3,4]
[3]*Institut des Sciences Moléculaires d'Orsay (ISMO), CNRS UMR 8214, Université Paris-Sud, Bâtiment 350, F-91405 Orsay cedex, France*
[4]*Synchrotron SOLEIL, L'Orme des Merisiers, Saint Aubin, Boîte Postale 48, F-91192 Gif-sur-Yvette cedex, France*

E. Robert, X.-J. Liu, C. Nicolas, and C. Miron
Synchrotron SOLEIL, L'Orme des Merisiers, Saint Aubin, Boîte Postale 48, F-91192 Gif-sur-Yvette cedex, France
(Received 8 March 2012; published 11 April 2012)

Absolute photoionization cross sections of Ar^+, Ar^{2+}, and Ar^{3+} ions have been measured in the 250–280 eV photon energy range. These results are compared to theoretical cross sections extracted from two new calculations we performed. They reproduce well the general behavior of the experimental spectra and the magnitude of the direct photoionization cross sections. However, the oscillator strength of the resonant structure in the spectra, dominated by $2p \rightarrow 3d$ transitions, is overestimated up to 80% by our calculations.

DOI: 10.1103/PhysRevA.85.043408 PACS number(s): 32.80.Fb, 32.80.Zb

I. INTRODUCTION

Beyond its fundamental interest, photoionization of ions is particularly important for fields such as astrophysics and stellar modeling, planetary science, and more generally for all laboratory plasma applications as well as industrial research. As an example, the solar radiative-convective boundary has been localized with high accuracy from helioseismic measurements [1]. However, theoretical results from the standard stellar model presently disagree with the experimental results, and one possible explanation is inadequate mid-Z element opacities in the 300–1500 eV photon energy range [2]. Photoionization is one of the elementary processes involved in an opacity calculation, and absolute photoionization cross-section measurements are crucial to validate the atomic data used in spectral opacity calculations. The merged-beam technique is commonly used for the experimental study of these processes, being particularly well suited for the determination of absolute photoionization cross sections. The basic requirement for such experiments is a high-photon flux to compensate for the very low density of the ionic targets (typically 10^5 ions/cm^3). Most of the experiments using this technique have been performed in the low-photon energy range (below 200 eV), except studies on K-shell photoionization of C^+ to C^{3+} ions [3–5], N^+ ion [6], O^+ ion [7], and Ne^+ to Ne^{3+} ions [8,9]. As a consequence, mainly studies on the photoionization processes of the outer shells of low-charged ions have been performed [10,11].

Despite the importance of argon ions in astrophysical [12] and laboratory plasmas [13,14], only a few measurements have been performed on the photoionization of these ions. Kravis *et al.* [15,16] have obtained the charge distribution of the photoions formed by broadband irradiation with synchrotron light of Ar^{2+} ions stored in a Penning trap. More recently, two works have been reported: one on the valence-shell photoionization of Ar^+ ion using the merged-beam technique [17], and the other on Ar^{8+} ions using an electron beam ion trap (EBIT) [18].

In this paper, we present results on the photoionization processes in the L inner shell of Ar^+ to Ar^{3+} ions. Our absolute measurements, obtained with the merged-beam technique, are compared to previous theoretical results, as well as new ones we obtained using a multiconfiguration Dirac-Fock (MCDF) code and the OPAS code dedicated to opacity calculations of hot and dense plasmas.

II. EXPERIMENTAL PROCEDURE

The experiment was performed on the MAIA setup permanently attached to the branch A of the PLEIADES beam line [19] at the French synchrotron radiation facility SOLEIL. In the 250–300 eV energy range used in the present work, the photons are produced by an Apple II permanent magnet 80 mm period undulator, then energy selected using a 400 lines/mm plane grating with varied groove depth (VGD) and varied line spacing (VLS). The spectral purity is provided by an appropriate combination of quasiperiodic design for the undulator and the use of the VGD for the grating to reduce diffraction efficiency of higher diffraction orders as compared to the first order. Typical flux at 250 eV photon energy measured at the exit of branch A with a calibrated photodiode is 1×10^{12} photons/s in 140 meV bandwidth. The photon energy calibration was ensured by absorption measurements using a gas cell based on the known energies of the Ar $2p \rightarrow nl$ [20] and Kr $3d \rightarrow nl$ [21] photoexcitation lines. Correction for the Doppler shift resulting from the target ion velocity is also performed. The accuracy on the energy calibration is estimated to be 40 meV.

*jean-marc.bizau@u-psud.fr
†Present address: Laboratoire de Physique Pharmaceutique, CNRS UMR 8612, Université Paris-Sud, Faculté de Pharmacie, 5 rue Jean-Baptiste Clément, 92296 Châtenay-Malabry, France.

A detailed description of the MAIA setup can be found in Ref. [6]. Briefly, the Ar ions are produced by heating argon gas in a 12.6 GHz permanent magnet electron cyclotron resonance ion source (ECRIS). The ions are extracted by applying a 4 kV positive voltage to the ion source, and are selected following their mass-to-charge ratio by a dipole magnet. After collimation by two sets of slits, the ion beam is merged with the monochromatized photon beam with the help of a spherical electrostatic deflector. The ions' charge after the interaction is analyzed by a second dipole magnet. The parent ions are collected in a Faraday cup. Typical current of target ions in the interaction region was of the order of 120 nA. The ions that have gained one or several charges during the interaction (also called photoions) go through an electrostatic deflector, used as a velocity filter, before being counted by microchannel plates. One goal of the velocity filter is to reduce the background signal mainly produced by collisional ionization of the parent ions with the residual gas in the interaction chamber, or by autoionization taking place during the flight time of the ions produced in metastable excited states in the ECRIS. A chopper, located at the exit of the photon beam line, allows subtracting of this background signal from the total signal recorded by the microchannel plates.

At a given photon energy, the photoionization cross sections σ are determined from the photoion count rate S using the formula

$$\sigma = \frac{Se^2\eta v q}{IJ\varepsilon \int_0^L \frac{dz}{\Delta x \Delta y F(z)}}, \tag{1}$$

where e is the charge of the electron, q the charge of the target ions and v their velocity, I and J are the current of photons and ions, respectively, and η and ε are the efficiency of the microchannel plates and of the photodiode, respectively. $\Delta x \Delta y F(z)$ is an effective beam area (z is the propagation axis of the two beams), where F is the two-dimensional form factor determined using three sets of xy scanners placed at each end and in the middle of the interaction region. Each scanner is a 0.2-mm-width slit moved across the ion and the photon beams. The length L of the interaction region is fixed by applying a positive bias (typically 600 V) on a 50-cm-long tube placed in the interaction region. In such a way, the photoions produced inside and outside the tube have different velocities and can be discriminated. The accuracy of the measured cross sections is determined by the statistical fluctuations of the photoion and noise counting rates, plus a systematic contribution resulting from the measurement of the different parameters in Eq. (1). The latter is estimated to be 15% and is dominated by the uncertainty on the determination of the photon flux, the form factor, and detector efficiency.

To record the photoionization spectra, two modes have been used. One with all the parameters of Eq. (1) recorded except the interaction length L, applying no voltage on the interaction tube. Since the whole interaction length of the beams is used, this mode offers the best statistics, allowing us to scan the photon energy with a smaller step (30 meV). However, only relative cross sections are obtained in this mode. In the second mode, the bias is applied to the tube to properly define the interaction length L, allowing for the determination of the cross sections in absolute value. A larger energy step (100 meV) is used in this mode. The spectra recorded in the first mode are then normalized in absolute value on those recorded in the absolute mode assuming the same integrated area.

III. THEORY

We performed MCDF calculations using the code developed by J. Bruneau [22]. Calculations are based on a full intermediate coupling in the j-j basis. Photoexcitation and direct photoionization cross sections are computed separately using both the length and velocity forms of the electric-dipole operator. The photoexcitation cross sections we calculate are always higher when the velocity form of the electric-dipole operator is used, by a factor of 1.21, 1.003, and 1.02 for Ar^+, Ar^{2+}, and Ar^{3+}, respectively. In the following, we will present only the results obtained in the Babushkin gauge, which corresponds to the length form in a nonrelativistic calculation [23]. Only the electric-dipole transitions have been considered. The Slater's transition state method has been used to optimize the one-electron wave functions [24]. The $2p$ photoexcitation cross sections have been evaluated for all levels of the $1s^2 2s^2 2p^6 3s^2 3p^q$ ground configurations ($q = 5$, 4, and 3 for Ar^+, Ar^{2+}, and Ar^{3+} ions, respectively). For each ionic stage, the $1s^2 2s^2 2p^5 3s^2 3p^q ns$ ($n = 4, \ldots, 7$) and $1s^2 2s^2 2p^5 3s^2 3p^q nd$ ($n = 3, \ldots, 7$) configuration sets have been considered to describe the photoexcited states taking into account configuration interactions. The level-to-level photoionization cross sections for ionizing a $2p$ electron from the ground configuration have been calculated for Ar^+ and Ar^{2+} ions, omitting configuration interactions for both the initial and the final ionized states. Photoionization cross sections have been calculated for photon energies up to 300 eV.

We also used the OPAS code [25] to calculate the photoabsorption cross section from the ground configuration of Ar^+, Ar^{2+}, and Ar^{3+} ions, in the 250–300 eV photon energy range. The OPAS code has been developed for opacity calculations. Only electric-dipole transitions are accounted for bound-bound and bound-free processes, which are computed separately. For each ionization stage, radial functions for bound electrons are obtained from the ground configuration-average energy minimization using the optimized potential method [26]. The radial functions for free electrons are calculated in the same optimized potential. The length form of the electric-dipole operator is used to calculate photoexcitation and photoionization processes. Direct photoionization cross sections for $2p$, $3s$, and $3p$ subshells are evaluated using the configuration-average distorted-wave approximation. The energy thresholds are evaluated from the initial and final configuration-average energies independently minimized. The photoexcitation cross sections involving $2p \rightarrow ns, nd$ transitions have been calculated for principal quantum number up to 7. For each pair of configurations connected by an electric-dipole transition, the total oscillator strength is evaluated. This value is used to normalize tabulated level-to-level oscillator strengths extracted from MCDF calculations neglecting configurations interaction. Tabulated data are calculated using the Babushkin gauge. This normalization allows preserving of the oscillator strength sum rule.

Both for MCDF and OPAS calculations, a Lorentzian profile is used for each line shape, with a full width at half maximum (FWHM) depending on the autoionization rates. The OPAS code has been used to estimate these rates. For each ionization stage, radial functions computed in the optimized potential of the $1s^2 2s^2 2p^5 3s^2 3p^q 3d$ photoexcited configurations are used. Assuming statistical populations for the ground configuration levels, a theoretical spectrum is synthesized for each ionization stage by summing weighted level-to-level cross sections. To compare with experimental results, theoretical spectra were convoluted with a Gaussian function to account for the finite spectral resolution.

IV. RESULTS AND DISCUSSION

The cross sections we experimentally determined for Ar^+, Ar^{2+}, and Ar^{3+} target ions are presented in Figs. 1–3, respectively. Single, double and, in the case of Ar^+ ion, up to triple photoionization cross sections have been recorded. The gray bars on each spectrum indicate the statistical uncertainty. The weakest channels, the triple ionization of Ar^+ ion and double ionization of Ar^{3+} ion, were recorded in the relative mode only. They have been normalized in absolute value assuming an identical form factor as the one recorded in relative mode for the single photoionization spectra of the same ion. Carbon contamination of the optics of the beam line has restricted the upper limit of our measurements to 282 eV photon energy.

The resonant structures observed in all the spectra result from $2p \rightarrow nd$, $(n+1)s$ photoexcitations, leaving the ions in $1s^2 2s^2 2p^5 3s^2 3p^q nd$, $(n+1)s$ highly excited states. Autoionization decay of these states leads to the single ionization channel, while the Auger decay produces the multiple-ionization

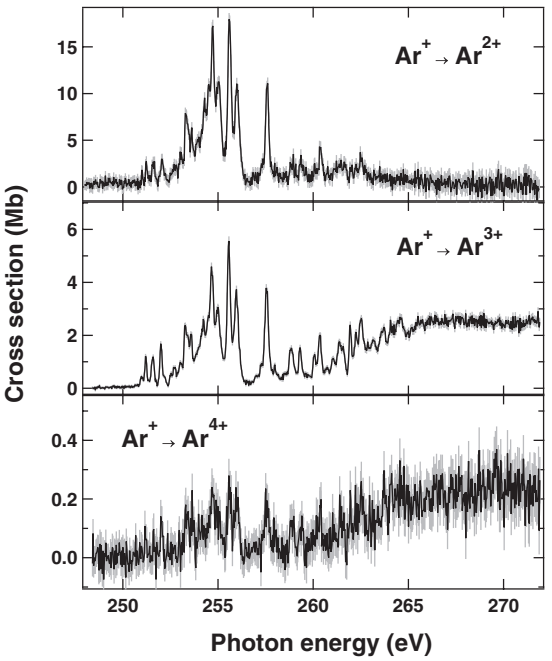

FIG. 1. Variation in the experimental photoionization cross sections of Ar^+ ion as a function of photon energy (from top to bottom: single, double, and triple photoionization cross section). The error bars in gray represent the statistical uncertainty.

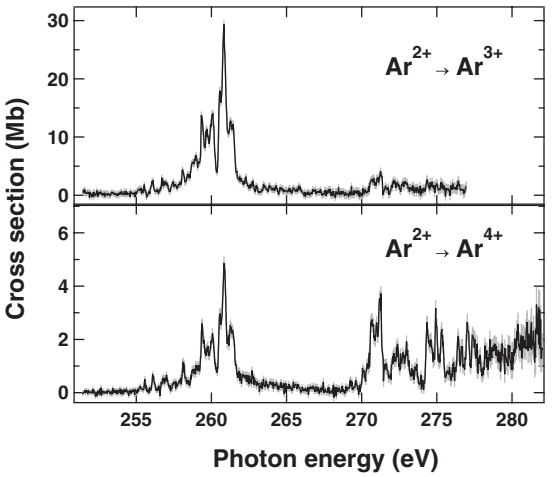

FIG. 2. Variation in the experimental photoionization cross sections of Ar^{2+} ion as a function of photon energy (from top to bottom: single and double photoionization cross section). The bars in gray represent the statistical uncertainty.

spectra. The general behavior of the spectra for the three ions clearly departs from the photoabsorption spectrum of neutral argon, which exhibits relatively weak and regular $2p \rightarrow nd$, $(n+1)s$ Rydberg series converging to the L_2 and L_3 edges [21,27,28]. For each ion stage, the presence of additional $3p$ hole(s) in the initial state strongly increases the number of $1s^2 2s^2 2p^5 3s^2 3p^q nd$, $(n+1)s$ excited states which can be reached via dipolar transitions. In addition, the collapse of the $3d$ orbital in presence of the hole in the $2p$ subshell is enhanced, increasing the $3p$-$3d$ interaction and leading to a redistribution of the oscillator strength to $2p \rightarrow 3d$ transitions [29].

The complexity of the spectra is increased in our measurements by the probable presence of ions in excited states in the ionic targets. They are produced in the ECRIS, and all metastable excited states with a lifetime longer than the time-of-flight of the ions between the ion source and the interaction region (a few μ sec) contribute to the spectra. In

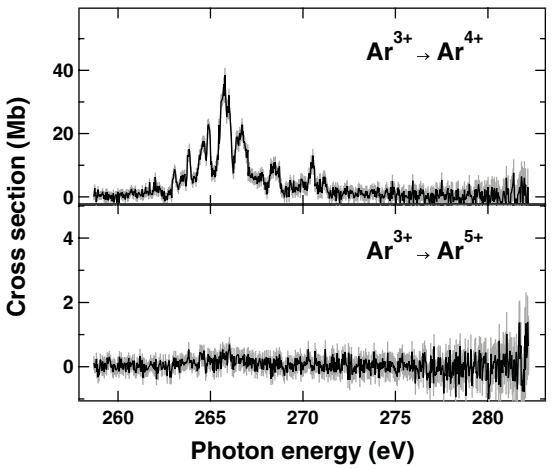

FIG. 3. Variation in the experimental photoionization cross sections of Ar^{3+} ion as a function of photon energy (from top to bottom: single and double photoionization cross section). The bars in gray represent the statistical uncertainty.

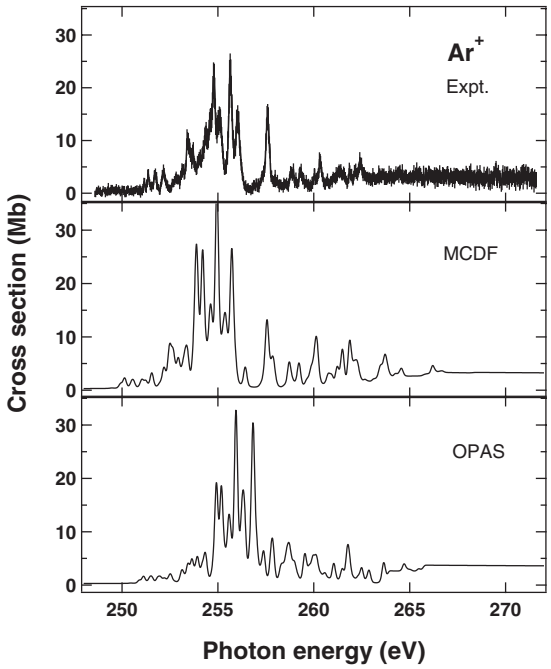

FIG. 4. Comparison of the experimental total cross section (top panel) for Ar^+ ion to the theoretical spectra reconstructed from the cross sections calculated using the MCDF (middle panel) and the OPAS (bottom panel) codes. The gray bars give the total uncertainty on the experimental data.

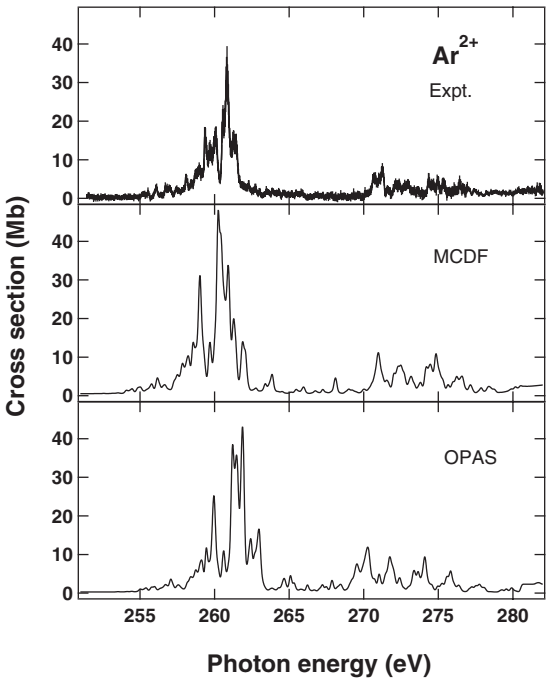

FIG. 5. Comparison between the experimental total cross section (top panel) for Ar^{2+} ion and the theoretical spectra reconstructed from the cross sections calculated using the MCDF (middle panel) and the OPAS (bottom panel) codes. The gray bars give the total uncertainty on the experimental data.

particular, this is the case for all the excited terms with the same configuration as the ground state. Some levels of the first excited $3p^{-1}3d$ configuration can also contribute, as the $3p^4$ (^3P) $3d$ ^4D term and $^4F_{9/2,7/2}$ levels of Ar^+ ion, and the $3p^2$ (^2P) $3d$ $^4F_{9/2,}$ $^4D_{7/2}$ levels of Ar^{3+} ion [30].

To the best of our knowledge, no calculations of the resonant photoionization cross sections for the $2p$ subshell of argon ions have been performed up to now. L-shell excitation effects are not included in the data available in the TOPBase [31]. In Figs. 4–6 we compare our experimental data (upper panels) with the photoionization spectra calculated using the MCDF code (middle panels) and the OPAS code (lower panels). For each ionic stage, the experimental data are obtained from the sum of all single and multiple ionization channels previously presented in Figs. 1–3. The gray bars give the total uncertainty on the measurements. In both calculations, only the contribution of the metastable terms with the same configuration as the ground level has been included. To reconstruct the theoretical spectra from the calculated individual photoionization cross sections, a statistical population of the terms has been assumed. A natural width of 63, 46, and 28 meV was applied to all the lines of Ar^+, Ar^{2+}, and Ar^{3+}, respectively. These values are significantly lower than for neutral argon, measured between 110 and 140 meV [20]. The spectra were convoluted with a 140 meV FWHM Gaussian profile to account for the experimental broadening. For all three ions, both calculations reproduce qualitatively well the experimental spectra. As expected, the position of the $2p \rightarrow 3d$ structures and the general behavior of the higher $2p \rightarrow nl$, $n > 3$ transitions are better reproduced by the MCDF results. However, both calculations systematically overestimate the intensity of the dominant structure, corresponding mainly to $2p \rightarrow 3d$ transitions. One reason might be the strong configuration interaction effects due to the collapse of the $3d$ orbital that are not correctly

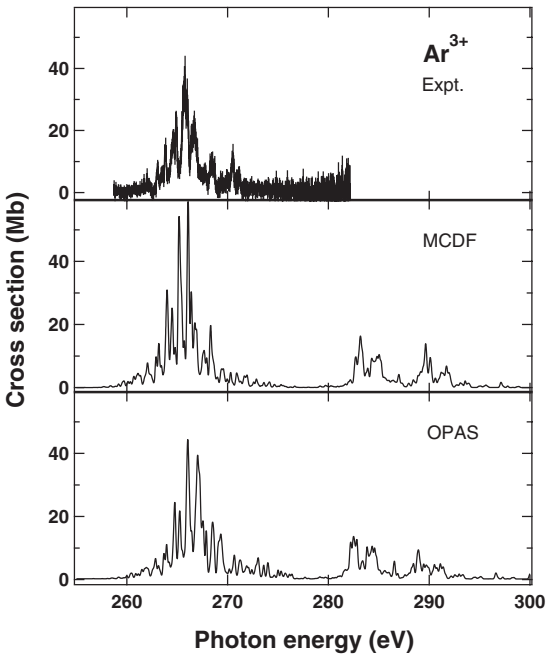

FIG. 6. Comparison of the experimental total cross section (top panel) for Ar^{3+} ion to the theoretical spectra reconstructed from the cross sections calculated using the MCDF (middle panel) and the OPAS (bottom panel) codes. The gray bars give the total uncertainty on the experimental data.

TABLE I. Experimental (second column) and calculated (MCDF: third column; OPAS: fourth column) integrated oscillator strength of the prominent structure corresponding mainly to the $2p \rightarrow 3d$ transitions. The branching ratio to the single, double, and triple ionization decay channels are given in the last three columns, respectively. The values for neutral argon are from Ref. [27].

	$2p \rightarrow 3d$ oscillator strength			Branching ratio (%)		
	Expt.	MCDF	OPAS	Single	Double	Triple
Ar				61	31	8
Ar^+	0.395	0.554	0.440	75	24	1
Ar^{2+}	0.470	0.851	0.739	84	16	
Ar^{3+}	0.782	1.097	1.070	99	1	

described in the calculations, and in particular by the OPAS code that neglects such effects. Photoionization from the $3p^{-1}3d$ metastable states, not included in the calculations, can also contribute to the discrepancy.

Recent multicoincidence electron spectroscopy studies of the Auger decay of the $2p$ hole in neutral argon have shown that the single Auger decay is the dominant route, leading mainly to the double ionization channel with an ion with two holes in the $3p$ subshell [32]. In the case of the resonant Auger process, a smaller contribution of Ar^{2+} $1s^22s^22p^53s^23p^4nd$, $(n+1)s$ excited state with the electron on the nd, $(n+1)s$ excited orbitals behaving like a spectator is also observed [33]. The triple ionization channel represents less than 10% of the total Auger decay, and is dominated by sequential Auger decay involving Ar^{2+} $3p^23d^2$ intermediate states [32,34]. A smaller contribution of direct double Auger emission is also observed. The direct double Auger spectrum is observed to be very similar to the normal Auger spectrum, with a dominant contribution of Ar^{3+} $3p^{-3}$ channel.

The experimental and calculated oscillator strengths obtained from the integration of the main structure observed on the spectra of Figs. 4–6, corresponding mainly to the $2p \rightarrow 3d$ transitions, are reported in Table I. The branching ratio to the single, double, and triple ionization decay channels is also given. The values for the neutral argon are taken from Samson *et al.* [27]. Our spectra on argon ions can be interpreted on the basis of neutral argon observations. Single photoionization is the dominant channel for all ionization stages. Its main population pathway is the autoionization decay of the $1s^22s^22p^53s^23p^qnd$, $(n+1)s$ excited states, leaving an ion with two additional holes in the $3p$ subshell:

$$2p^53s^23p^qnd, \quad (n+1)s \rightarrow 2p^63s^23p^{(q-2)}nd, \quad (n+1)s + e^-. \tag{2}$$

Multiple ionization channels are dominated by cascade Auger decays involving $3s^{-1}$ satellites or $3s^{-2}$ intermediate states:

$$2p^53s^23p^qnd, \quad (n+1)s \rightarrow 2p^63s3p^{(q-1)}nd, \quad (n+1)s + e^- \rightarrow 2p^63s^23p^{(q-2)} + e^-. \tag{3}$$

For increasing charge of the ionic target, we note the spectacular increase of the oscillator strength, associated with the gradual collapse of the $3d$ orbital, and the vanishing contribution of the Auger decay channels, which reflects the decrease of the number of intermediate states available for the cascade Auger process. Both calculations qualitatively reproduce the increase of the oscillator strength but, as previously mentioned, clearly overestimate its intensity, by up to 80% in the case of the Ar^{2+} ion. Let's note this discrepancy cannot be accounted for by radiative decay of the intermediate states. We calculated the ratio of average autoionization rates over average radiative rates to be 4757, 1877, and 659 for Ar^+, Ar^{2+}, and Ar^{3+}, respectively.

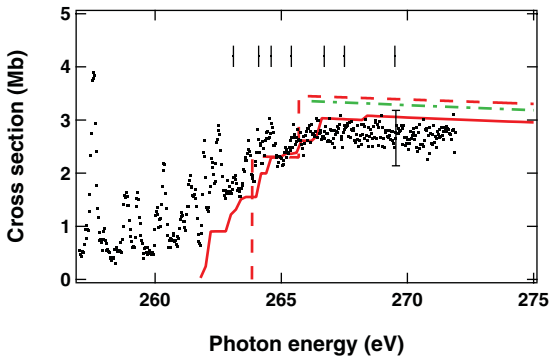

FIG. 7. (Color online) Comparison of the experimental total photoionization cross section for Ar^+ ion (dots) to the direct $2p$ photoionization cross section calculated by Verner and Yakovlev [35] (dashed-dotted line), the MCDF code (continuous line), and the OPAS code (dashed line). The vertical bars give the position of the $2p$ thresholds measured by Lablanquie *et al.* [33]. Typical total uncertainty of the measurements is shown by the error bar at 270 eV photon energy.

In the case of Ar^+ ion, we observe above 263 eV photon energy (Fig. 4) a flat and slowly decreasing continuum, corresponding to the direct photoionization in the $2p$ subshell. It is only visible in the double and triple ionization channels because of the fast Auger decay of the hole in the $2p$ subshell (see Fig. 1). An enlargement of Fig. 4 in this photon energy range is given in Fig. 7. The experimental cross section (dots) is compared to the results of our MCDF (continuous line) and OPAS (dashed line) calculations for the direct photoionization process, as well as to the previous Dirac-Fock (DF) calculations of Verner and Yakovlev [35]. The steps in the MCDF cross section reflect the opening of the various $2p$ thresholds starting from the two initial levels $^2P_{3/2,\,1/2}$. An electron coincidence experiment has determined the position of the first $2p$ threshold at 263.1 eV for the Ar^+ ion in the ground state [36], in between the MCDF and OPAS calculated values, 262.0 and 265.7 eV, respectively. It is not possible to precisely determine the position of the ionization thresholds from our measurements since there is no clear frontier in the spectra between the direct ionization channels and the Rydberg series converging to the thresholds. Above the thresholds, the MCDF calculations give the best agreement with the experimental data. At 270 eV photon energy, the measured cross section is 2.8 ± 0.5 Mb, with a relative intensity of 5% in the single-, 86% in the double-, and 9% in the triple-ionization channels. This cross section is significantly lower than for neutral argon, measured to be 4.6 ± 0.5 Mb at the L_2 threshold, but the branching ratios to the different ionization channels are close: 9%, 78%, and 12% for single,

double, and triple ionization, respectively [27]. For Ar^{2+} ion, our measurements stop just above threshold and indicate a value around 1.9 Mb in the double ionization channel, slightly lower than for Ar^{+} ion.

V. CONCLUSION

In this paper, we have presented results on the photoionization in $2p$ subshell of Ar^{+} to Ar^{3+} ions. Single, double, and up to triple ionization channels in the case of Ar^{+} ion, have been measured in the 250–280 eV photon energy range. The measurements have been compared to theoretical spectra reconstructed from the cross sections calculated using a MCDF code and the OPAS opacity code. Both calculations reproduce qualitatively well the resonant photoionization spectra, but tend to overestimate by 10% to 80% the intensity of the main structure, dominated by $2p \rightarrow 3d$ transitions. Overestimation of the calculated cross sections was already observed in the case of the $3p \rightarrow 3d$ transitions for the first ions of the iron isonuclear sequence [37].

[1] S. Basu, Mon. Not. R. Astron. Soc. **298**, 719 (1998).
[2] S. Basu and H. M. Antia, Phys. Rep. **457**, 217 (2008).
[3] A. S. Schlachter, M. M. Sant'Anna, A. M. Covington, A. Aguilar, M. F. Gharaibeh, E. D. Emmons, S. W. J. Scully, R. A. Phaneuf, G. Hinojosa, I. Álvarez, C. Cisneros, A. Müller, and B. M. McLaughlin, J. Phys. B: At. Mol. Opt. Phys. **37**, L103 (2004).
[4] S. W. J. Scully, A. Aguilar, E. D. Emmons, R. A. Phaneuf, M. Halka, D. Leitner, J. C. Levin, M. S. Lubell, R. Püttner, A. S. Schlachter, A. M. Covington, S. Schippers, A. Müller, and B. M. McLaughlin, J. Phys. B: At. Mol. Opt. Phys. **38**, 1967 (2005).
[5] A. Müller, S. Schippers, R. A. Phaneuf, S. W. J. Scully, A. Aguilar, A. M. Covington, I. Álvarez, C. Cisneros, E. D. Emmons, M. F. Gharaibeh, G. Hinojosa, A. S. Schlachter, and B. M. McLaughlin, J. Phys. B: At. Mol. Opt. Phys. **42**, 235602 (2009).
[6] M. F. Gharaibeh, J. M. Bizau, D. Cubaynes, S. Guilbaud, N. El Hassan, M. M. Al Shorman, C. Miron, C. Nicolas, E. Robert, C. Blancard, and B. M. McLaughlin, J. Phys. B: At. Mol. Opt. Phys. **44**, 175208 (2011).
[7] K. Kawatsura, H. Yamaoka, M. Oura, T. Hayaishi, T. Sekioka, A. Agui, A. Yoshigoe, and F. Koike, J. Phys. B: At. Mol. Opt. Phys. **35**, 4147 (2002).
[8] H. Yamaoka, M. Oura, K. Kawatsura, T. Hayaishi, T. Sekioka, A. Agui, A. Yoshigoe, and F. Koike, Phys. Rev. A **65**, 012709 (2001).
[9] M. Oura, H. Yamaoka, K. Kawatsura, J. Kimata, T. Hayaishi, T. Takahashi, T. Koizumi, T. Sekioka, M. Terasawa, Y. Itoh, Y. Awaya, A. Yokoya, A. Agui, A. Yoshigoe, and Y. Saitoh, Phys. Rev. A **63**, 014704 (2000).
[10] J. B. West, J. Phys. B: At. Mol. Opt. Phys. **34**, R45 (2001).
[11] H. Kjeldsen, J. Phys. B: At. Mol. Opt. Phys. **39**, R325 (2006).
[12] T. Lanz, K. Cunha, J. Holtzma, and I. Hubeny, Astrophys. J. **678**, 1342 (2008).
[13] X. M. Zhu and Y. K. Pu, J. Phys. D: Appl. Phys. **43**, 403001 (2010).
[14] H. J. N. van Eck, T. A. R. Hansen, A. W. Kleyn, H. J. van der Meiden, D. C. Schram, and P. A. Zeijlmans van Emmichoven, Plasma Sources Sci. Technol. **20**, 045016 (2011).
[15] S. D. Kravis, D. A. Church, B. M. Johnson, M. Meron, K. W. Jones, J. C. Levin, I. A. Sellin, Y. Azuma, N. Berrah-Mansour, H. G. Berry, and M. Druetta, Phys. Rev. Lett. **66**, 2956 (1991).
[16] S. D. Kravis, D. A. Church, B. M. Johnson, M. Meron, K. W. Jones, J. C. Levin, I. A. Sellin, Y. Azuma, N. Berrah-Mansour, H. G. Berry, and M. Druetta, Phys. Rev. A **45**, 6379 (1992).
[17] A. M. Covington, A. Aguilar, I. R. Covington, G. Hinojosa, C. A. Shirley, R. A. Phaneuf, I. Álvarez, C. Cisneros, I. Dominguez-Lopez, M. M. Sant'Anna, A. S. Schlachter, C. P. Ballance, and B. M. McLaughlin, Phys. Rev. A **84**, 013413 (2011).
[18] M. C. Simon, M. Schwarz, S. W. Epp, C. Beilmann, B. L. Schmitt, Z. Harman, T. M. Baumann, P. H. Mokler, S. Bernitt, R. Ginzel, S. G. Higgins, C. H. Keitel, R. Klawitter, K. Kubiček, V. Mäckel, J. Ullrich, and J. R. Crespo López-Urrutia, J. Phys. B: At. Mol. Opt. Phys. **43**, 065003 (2010).
[19] E. Robert, X.-J. Liu, C. Nicolas, and C. Miron, http://www.synchrotron-soleil.fr/portal/page/portal/Recherche/LignesLumiere/PLEIADES; O. Travnikova, J. C. Liu, A. Lindblad, C. Nicolas, J. Soderstrom, V. Kimberg, F. Gelmukhanov, and C. Miron, Phys. Rev. Lett. **105**, 233001 (2010); J. Söderström, A. Lindblad, A. Grum-Grzhimailo, O. Travnikova, C. Nicolas, S. Svensson, and C. Miron, New. J. Phys. **13**, 073014 (2011); T. D. Thomas, E. Kukk, K. Ueda, T. Ouchi, K. Sakai, T. X. Carroll, C. Nicolas, O. Travnikova, and C. Miron, Phys. Rev. Lett. **106**, 193009 (2011); C. Miron, C. Nicolas, O. Travnikova, P. Morin, Y. Sun, F. Gelmukhanov, N. Kosugi, and V. Kimberg, Nat. Phys. **8**, 135 (2012).
[20] M. Kato, Y. Morishita, M. Oura, H. Yamaoka, Y. Tamenori, K. Okada, T. Matsudo, T. Gejo, I. H. Suzuki, and N. Saito, J. Electron Spectrosc. Relat. Phenom. **160**, 39 (2007).
[21] C. G. King, M. Tronc, F. Read, and R. C. Bradford, J. Phys. B: At. Mol. Phys. **10**, 2479 (1977).
[22] J. Bruneau, J. Phys. B **17**, 3009 (1984).
[23] I. P. Grant, J. Phys. B **7**, 1458 (1974).
[24] J. C. Slater, *Quantum Theory of Molecules and Solids Spectral Lines*, Vol. IV (McGraw-Hill, New York, 1974).
[25] C. Blancard, P. Cossé, and G. Faussurier, Astrophys. J. **745**, 10 (2012).
[26] J. D. Talman and W. F. Shadwick, Phys. Rev. A **14**, 36 (1976).
[27] J. A. R. Samson, W. C. Stolte, Z. X. He, J. N. Cutler, and D. Hansen, Phys. Rev. A **54**, 2099 (1996).
[28] O.-P. Sairanen, A. Kivimäki, E. Nommiste, H. Aksela, and S. Aksela, Phys. Rev. A **54**, 2834 (1996).
[29] M. Meyer, E. von Raven, B. Sonntag, and J. E. Hansen, Phys. Rev. A **49**, 3685 (1994).
[30] C. Froese Fischer and G. Tachiev, MCHF/MCDHF Database, Version 2, Refs. No. 20 and 35; available online at http://physics.nist.gov/mchf (National Institute of Standards and Technology, 2011).
[31] W. Cunto, C. Mendoza, F. Ochdenbein, and C. Zeippen, Astron. Astrophys. **275**, L5 (1993).

[32] P. Lablanquie, L. Andric, J. Palaudoux, U. Becker, M. Braune, J. Viefhaus, J. H. D. Eland, and F. Penent, J. Electron Spectrosc. Relat. Phenom. **156–158**, 51 (2007).

[33] Y. Hikosaka, P. Lablanquie, F. Penent, P. Selles, T. Kaneyasu, E. Shigemasa, J. H. D. Eland, and K. Ito, Phys. Rev. A **80**, 031404(R) (2009).

[34] Y. Hikosaka, P. Lablanquie, F. Penent, T. Kaneyasu, E. Shigemasa, R. Feifel, J. H. D. Eland, and K. Ito, Phys. Rev. Lett. **102**, 013002 (2009).

[35] D. A. Verner and D. G. Yakovlev, Astron. Astrophys., Suppl. Ser. **109**, 125 (1995).

[36] P. Lablanquie, S.-M. Huttula, M. Huttula, L. Andric, J. Palaudoux, J. H. D. Eland, Y. Hikosaka, E. Shigemasa, K. Ito, and F. Penent, PhysChemChemPhys **13**, 18355 (2011).

[37] J.-M. Bizau, C. Blancard, D. Cubaynes, F. Folkmann, D. Kilbane, G. Faussurier, H. Luna, J. L. Lemaire, J. Blieck, and F. J. Wuilleumier, Phys. Rev. A **73**, 020707(R) (2006).